Recursive Spin System Characterization in one and two dimensions using Zero to Ultra-Lowfield Nuclear Magnetic Resonance at Natural Abundance

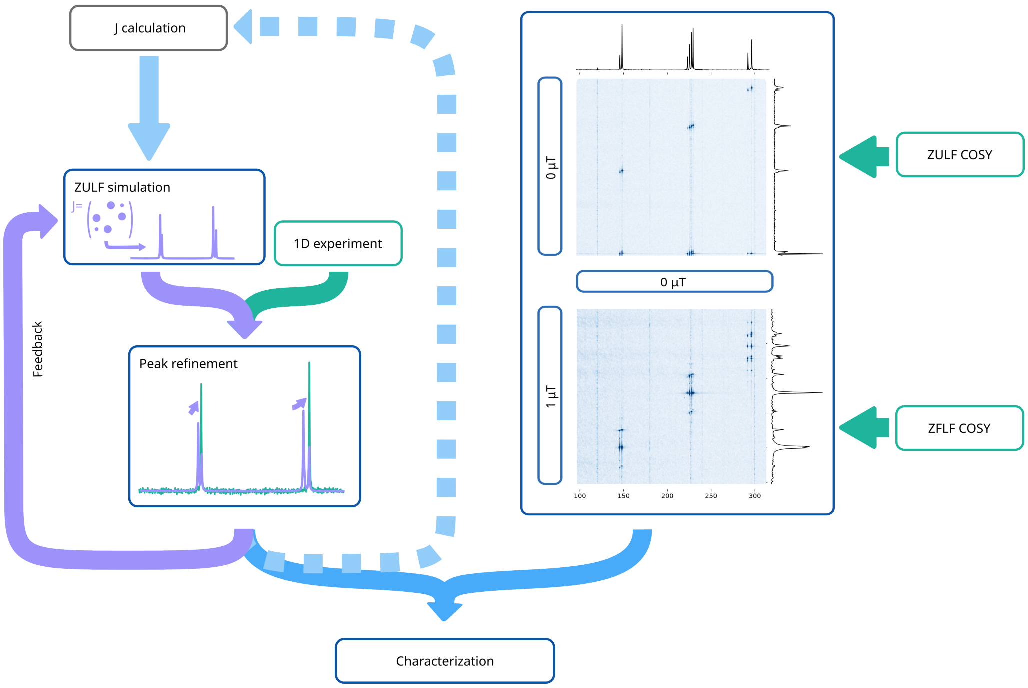

Raphael Zumbrunn
rzumbrunn@ethz.ch

Supervisors:
Prof. Dr. Alexander Barnes
alexander.barnes@phys.chem.ethz.ch
Prof. Dr. Ashok Ajoy
ashokaj@berkeley.edu

Advisor:
Blake Andrews
bca@berkeley.edu

Zürich, July 24, 2025

Raphael Zumbrunn

Bachelor Thesis
ETH Zürich/ UC Berkeley, HS24

To all those people who have and continue to stand up against fascism

Bachelor Thesis
ETH Zürich/ UC Berkeley, HS24

1 Abstract

Most modern applications of magnetic resonance take place in highly homogenous high-field magnets. Interactions of nuclei with this magnetic field are well understood and can be used to characterize a plethora of materials under study. Due to advances in magnetic shielding and magnetic sensors such as optically pumped magnetometers (OPM) a new avenue of magnetic resonance experiments has been opened. Zero to Ultra-Low Field (ZULF) NMR observes the evolution of spin systems under their untruncated J-coupling hamiltonian, leading to new types of spectra where the tools for analysis are much less developed. This work presents the development of such tools for ZULF NMR applied to compounds at natural abundance. A setup allowing for 2D experiments, as well as structured exploration of the parameter space was developed, for the first time opening the door to analysis in real world chemical contexts, where conventional NMR modalities are too costly or impractical. To allow for rapid prototyping and better interpretability an *in silico* replica of the experiment, modeling the evolution of the spin system from first principles and according to the real experiment, was created. Using a custom-built simulation algorithm, a gradient-based spectral refinement routine was built, allowing for extraction of underlying J values from experimental spectra. This work paves the way towards understanding and performing magnetic resonance experiments in the Ultra-Low to Zero Field regime, bringing the power of NMR to much broader practical applications.

2 Introduction

Magnetic resonance techniques such as nuclear magnetic resonance (NMR) and magnetic resonance imaging (MRI) are staples of modern chemical and material science, as well as medical research[1].[2] Both techniques rely on the transient magnetic properties of materials that have been excited by radio frequency pulses in strong magnetic fields. This necessitates extremely homogeneous magnetic fields ($> 10ppb$)[3] to avoid line broadening. Building such magnets is challenging and expensive, making both techniques, invaluable as they are, inaccessible in low-resource contexts. Zero to Ultra-Low Field (ZULF) NMR is a technique where detection is moved from high field to ultralow or zero field. This alleviates inhomogeneity broadening as it is much easier to reach homogeneity at zero field.[4] While polarization might still take place at high field, magnetic inhomogeneity there is now imprinted onto the amplitude, which is not relevant to broadening.

Due to the nature of the observables in the ZULF regime however, only heteronuclear compounds can be observed. In the context of organic chemistry this means that mostly molecules containing ^{13}C isotopes will be relevant to the spectra. For this reason the majority of prior ZULF literature has worked with isotope enriched compounds, which increases the abundance of ^{13}C from 1.1% to near 100%, increasing the signal-to-noise ratio (SNR) and cutting the measurement time by a factor of ≈ 8265. While useful for proof-of-principle and fundamental work we believe that the eventual goal of any analytical method needs to be the application to "off the shelf" molecules.

Working with improved sample geometries and using custom tools for parameter optimization this work manages to accomplish this feat for both the base as well as extended experiments. Introducing non-labeled compounds to ZULF NMR moves us another step closer to applications in real world contexts, specifically to contexts where standard NMR methods cannot be applied.

One such field is sensing through opaque containers. This is possible at ZULF due to the striking difference in the involved frequency scales, which are much lower ($\approx 5 - 500Hz$ vs $< 100MHz$), making the corresponding skin depth in conductive materials much larger,[5] enabling detection through containers, which can even be conductive.[6] This also allows study of liquids in porous materials[7] and heterogeneous/biphasic chemical reactions.[8]

The combination of these aspects make ZULF uniquely capable as a quality control tool. Its relaxed requirements on magnet homogeneity also enable benign cost scaling for multichannel implementations of ZULF NMR.[4]

There are however some hurdles to overcome before widespread implementation becomes plausible. One hurdle is the difficult interpretation of spectra. At high field, peaks are mostly independent of each other, which leads to easy local interpretations of the signal. This is due to the fact that HF spectra are dominated by the local, one-spin Zeeman hamiltonian, which truncates the J-coupling interaction. At zero field however the J-coupling hamiltonian remains untruncated, which leads to couplings that can span the entire molecule.[9] This makes the spectrum highly non-local[10] making them harder to interpret by hand. Moreover, a single spin system may lead to many peaks making the spectrum very complex and fingerprint-like.[9] Additionally, no databases for experimental ZULF spectra exist to date, which make referencing known compounds impossible.

In this paper we take two approaches to these interpretability issues. Using multidimensional ZULF spectroscopy, which was inspired by Nobel Prize winning research at high field,[11] we managed to reduce spectral complexity and allow better interpretability. To extend the formalism of multidimensional NMR from high field to ZULF a method analogous to the superoperator formalism was employed. From this treatment it is possible to derive the amplitude of peaks in the 2D ZULF experiment. As the ZULF environment allows for novel ways to manipulate the Hamiltonian during evolution a variety of new 2D experiments can be performed. Two special cases are analyzed in this paper; ZFLF COSY (Zero Field Low Field Correlation SpectroscopY) and (True) ZULF-COSY (Zero to Ultralow Field Correlation SpectroscopY). Those two methods differ essentially only in the hamiltonian which is applied during evolution time τ, giving rise to the indirect dimension. ZULF-COSY is a direct analogue to high-field COSY, giving rise to a symmetric spectrum. As opposed to HF-COSY, where cross peaks show J-coupling between spins,[12] ZULF-COSY shows spin system connectivity and coherence transfer.[13] This allows for the mapping of said spin systems. Later in this paper ZULF-COSY is used to distinguish isotope labels in isotopic mixtures. A mathematical derivation of the form of ZULF-COSY spectra can be found in the appendix B.2.

The other approach is using methods borrowed from deep learning[14] in concert with a *virtual replica* of the experiment to extract the fundamental physical values underlying the complicated spectrum. Using this, complex spectra can be reduced to their fundamental building blocks, the pairwise J-coupling strengths, which are easier to interpret. Those fundamental building block are also less dependent on the specific spectroscopic methodology, which means that such values can be found in established databases built for other experimental techniques.[15]

To understand how ZULF can give rise to this range of challenges and opportunities it makes sense to highlight the key conceptual differences between high-field (HF) and ZULF NMR.

In contrast to HF NMR, which observes evolution under the Zeeman Hamiltonian, ZULF NMR observes evolution under the J-coupling hamiltonian (see eq. i).[9]

$$\hat{H}_{ZULF} = \sum_{i,j} J_{ij} \hat{\boldsymbol{I}}_i \cdot \hat{\boldsymbol{I}}_j \tag{i}$$

Where J_{ij} is the isotropic pairwise J-coupling strength and $\hat{\boldsymbol{I}}_i$ is the spin vector operator of atom i.

It is important to note that this is not the same J-coupling operator found at high field, as H_{ZULF} represents the fully untruncated J-coupling interaction. The difference between $H_{J,HF}$ and H_{ZULF} is most directly evident by examining their respective symmetries.

Where $H_{J,HF} = \sum_{ij} J_{ij} \hat{I}_i^z \hat{I}_i^z$ has cylindrical symmetry around the z axis, H_{ZULF} is fully spherically symmetric due to the isotropic character of the hamiltonian. This difference is a direct consequence of the secular approximation, which is usually done at high field.[16] For more clarification around this point see B.3. The cylindrical symmetry and the localized nature of the Zeeman interaction at HF NMR motivates the description of the system in terms of eigenvalues of I_i^z. This basis is often called Zeeman basis and is simply a tensor product space of the individual spin angular momenta of the spins involved. For ZULF it makes sense to describe the system with operators that better capture the underlying symmetries of the energy eigenstates and the delocalized nature thereof.

The new states that are often chosen to describe the ^{13}C−H systems can be written as follows:

$$
\begin{aligned}
|S_0\rangle &= \frac{1}{\sqrt{2}}(|\uparrow\downarrow\rangle - |\downarrow\uparrow\rangle) \\
|T_1\rangle &= |\uparrow\uparrow\rangle \\
|T_0\rangle &= \frac{1}{\sqrt{2}}(|\uparrow\downarrow\rangle + |\downarrow\uparrow\rangle) \\
|T_{-1}\rangle &= |\downarrow\downarrow\rangle
\end{aligned}
$$

With $|S_0\rangle$ denoting the singlet state and $|T_i\rangle$ denoting the triplet states. Note that due to the $\hat{\boldsymbol{F}}$ symmetry the energy of all the triplet states is equivalent. This gives rise to one single transition at the frequency J, which is the ZULF spectrum for a $^{13}C-H$ system.

From the fact that the total spin is conserved it might at first seem contradictory that there would be any observable magnetization at ZULF. The only reasonable transition would be $|S_0\rangle \leftrightarrow |T_0\rangle$, but both of those states are seemingly non-magnetic. This observation is correct for homonuclear systems, where the magnetization and the spin of a system are directly related with each other. In the case of a heteronuclear system however the magnetization of the triplet and the singlet state can differ due to different γ on the two nuclei. For the case of ^{13}C−H the signal amplitude can be derived to be proportional to the differences in gamma. I.e. $A \propto (\gamma_C - \gamma_H)$.

This highlights another potentially interesting application of ZULF NMR for probing low γ nuclei, which are hard to detect at high field.

Similar arguments can be made for more complex spin systems, where we can use the Clebsh Gordan decomposition to find the multiplicities of the energy levels. To better elucidate this point, we will show the procedure on the example of a $CH2$ system. Starting with the tensor-product representation of the three spins interacting we can apply Clebsh Gordan first to the H-system, and then couple that system with the carbon.

$$
\begin{aligned}
S^C_{1/2} \otimes S^H_{1/2} \otimes S^H_{1/2} &= S^C_{1/2} \otimes (K^H_1 \oplus K^H_0) \\
&= (F^{CH}_{3/2} \oplus F^{CH}_{1/2}) \oplus F^{CH}_{1/2}
\end{aligned}
$$

During the coupling we introduce two new operators; K and F. With K representing the hydrogen spin, and F representing the total spin of the system. From this quick calculation we see that there is only one allowed transition ($F^{CH}_{3/2} \leftrightarrow F^{CH}_{1/2}$). The multiplicities can be calculated via $m = 2F + 1$, giving rise to the following energy structure (see fig 1) with a single transition at $\frac{3}{2}J$.

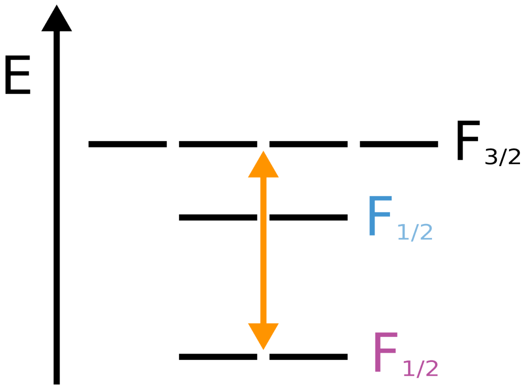

Figure 1: Energy level diagram of a $CH2$ system at Zero Field. The energy levels can be labeled by the total spin F, the multiplicity can then be calculated via $m = 2F + 1$. Only one transition is allowed (marked in orange). Evaluating the energy levels yields a transition frequency of $\frac{3}{2}J$.

3 Methods

In this work we closely integrated experiment and simulation to allow for quick experiment design and implementation. The simulation acts as a *virtual replica* of the real setup and mirrors many of its features including the same configuration file format.

3.1 Experiment

A ZULF experiment consists of three phases in which a sample is exposed to varying B-fields (see fig 2). In the preparation phase a sample is polarized. It is then subsequently transported to the ZULF regime, where the state is manipulated by application of direct current (DC) B-field pulses. The resulting state is then detected.

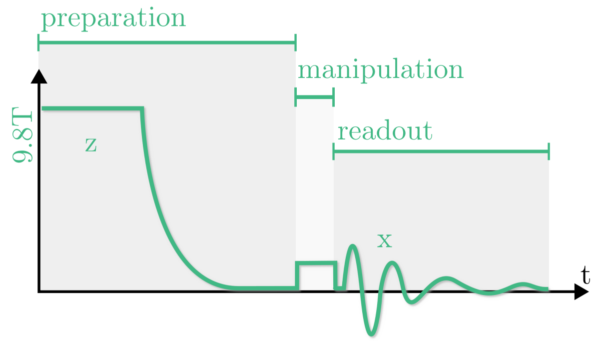

Figure 2: Generic ZULF experiment. A state is polarized at high field and then shuttled to low field, where a sequence of pulses can be applied. Afterwards the pulses the oscillating magnetic field can be picked up. Due to spatial constraints the polarization and measurement axis are along z and x respectively, necessitating either adiabatic or pulsed reorientation during the manipulation phase.

Base experiment

In our specific implementation the sample is polarized in a $9.4T$ wide bore horizontal superconducting magnet, which would normally be too inhomogeneous for conventional NMR. It is then quickly ($> 1s$) shuttled to the center of a TWINLEAF MS-2 mu-metal magnetic shield.[17] The layered mu-metal structure enables access to fields very close to zero ($< 10nT$). The direction of the transient magnetic field is then rotated by application of an orthogonal Helmholtz pulsing coil, which is integrated into the shield. The resulting states' coherent evolution under its J-coupling Hamiltonian is then observed using a QuSpin QZFM optically pumped magnetometer (OPM).[18] For the base experiment readers are referred to previous work in this group by Andrews et al..[4] Based on this setup a few changes were applied to increase reliability and allow for a better signal-to-noise ratio (SNR).

Improvements

To counteract the inherently low sensitivity of ZULF experiments the base setup was extended to replace the standard NMR tubes with Gas Chromatography vials, which are better suited to the OPM geometry. The Gas Chromatography (GC) vials also have a larger volume which contributes to the stronger signal. However, a next iteration with less tall GC vials is believed to have similar signal properties with less sample[a]. One other change was the shuttling software, which was modified to include a self-homing stage to counteract shuttle position drift. Because the homing is performed during polarization and because the polarization region is relatively large w.r.t the sample no time is lost during homing. Reducing experiment drift at no cost in signal strength or experiment time. Using these improvements among other operational improvements such as improved grounding a 16.4x improvement in SNR (which is an improvement of 270x in time) was attained. This improvement allows us to observe ZULF spectra of compounds at natural abundance. Additionally, the setup can run uninterrupted for multiple days without human intervention. This allows for longer experiments which would otherwise have been impractical. To coordinate those long-running experiments an experiment-design user interface (UI) was programmed using the UI library PyQt5.[19] The UI allowed for quick and easy generation of calibration curves, which were then run unattended for multiple days. This was a major contributing factor to the improvements in SNR.

3.2 Simulations

We created a full ZULF simulation library in python using NumPy, SciPy and QuTiP.[20,21,22] Our library supports identical input formats to the experimental setup allowing for parallel and iterative development of simulated and real sequences. This *in silico* replica of the experiment allows for full interoperability between experiment and simulation, yielding nearly exact equations of motion for the spin system at every step in the experiment shown in Fig. 2.

A custom optimized solver was written in NumPy to allow for quick spectral simulation ($< 5s$ vs $\approx 20min$). A pure NumPy approach was cho-

---

[a] This is on account of the sensor geometry. The GC vial can better fill the field of view of the detector, but also has a lot of volume to the sides of the sensor. This volume on the side is believed to only slightly contribute to the total signal amplitude.

sen to facilitate auto-differentiation via HIPS autograd.[23] Both the custom frequency-domain solver (see section 3.2 page 5) and the time domain master equation solver are accessible via the same interface allowing quick switching between simulation modes.[b] The ZULFPy simulation framework[24] can be roughly separated into three separate parts: Interface, Solver and Optimizer. In theory all three parts can work independently of each other and can be substituted if required. This allows for modular development of new capabilities without compromising the existing codebase.

Interface

The interface acts as a layer of abstraction between the user and the simulation. It acts as a bridge between the experimental configuration and the computational structure. By ingesting the same configuration and sequence files[c] as the experiment, sequences can be rapidly developed *in silico* and directly deployed to the real setup. The code is fully compatible with Python 3.9 and can be run from a Jupyter notebook kernel[25] making it compatible with modern remote computing infrastructure provided by many institutions.[26] More information about the interface can be found in the supporting information B.

Solver

Simulations can be run using two parallel and independent frameworks. The more detailed, but less performant routine hooks into QuTiP[27,28,29] an open source library for simulation of open quantum systems. The QuTiP simulation takes relaxation effects via the Gorini-Kossakowski-Sudarshan-Lindblad (GKSL) equation into consideration (see eq. ii).

$$\dot{\rho} = \frac{1}{i\hbar}[H, \rho] + \sum_i \gamma_i \left(L_i \rho L_i^\dagger - \frac{1}{2} \left\{ L_i^\dagger L_i, \rho \right\} \right) \quad \text{(ii)}$$

Solving this equation using time discretization leads to results in the time domain, which can then be Fourier transformed into the desired spectrum. For the additional effort we are rewarded with model internal linewidths and relaxation dynamics.

For most of this paper the linewidths of the simulation were not taken into consideration. This enabled a much easier and more efficient approach to the simulation: Diagonalization. For mathematical details see SI B.2.

Neglecting dissipative and decoherence terms in the calculation of energy levels gives us two main advantages. On one hand the preparation of the initial state can be simply modeled via a concatenation of unitary evolutions, which can be efficiently computed via diagonalization. Additionally, the diagonalized Hamiltonian lends itself to interpretation in the energy/frequency domain. We can therefor skip the fourier transform step originally required saving on additional computing power.

Optimizer

Integrating simulations with experimental data can be a challenging task as it requires (partially) solving the inverse problem to obtain good simulation parameters, in our case the pairwise J-coupling values. Those pairwise J-coupling values can be represented as an adjacency matrix, where the entry at i, j symbolizes the J-coupling between spin i and spin j. Previous work has obtained simulation parameters from high field NMR studies, which were then refined by hand.[30] While this method produces very good spectral overlap it is labor-intensive and does not scale well to larger systems due to the number of parameters growing as n^2, where n is the number of involved atoms.

For this reason a feedback refinement scheme inspired by machine learning techniques was developed. Using gradient based minimization methods, a spectral loss function that characterizes experimental fit can be optimized. Perfect spectral overlap will be indicated by a minimum in the loss function.

To show stability and convergence an ensemble of slightly perturbed starting values is optimized. Every element of the ensemble will converge to a local minimum. Given enough ensemble elements it is assumed a global optimum can be found.

---

[b] Currently, gradient based optimization is only supported for the diagonal solver

[c] The experiment is controlled by a structured text file, that specifies which channels, motors and sensors should be activated at which part of the experiment. This is the basis for reproducible and parametrizable experiments.

3.3 Tools

To enable rapid prototyping of sequences and generation of multi-parameter experiments an experiment-generation user interface (UI) was created. The UI allows for easy creation of N-dimensional experiments, which are invaluable during experiment calibration, where signal is optimized w.r.t a plethora of parameters. To sample the parameter space efficiently an iterative sampling strategy was developed, which first samples a course grid, which is then refined in subsequent steps 3.

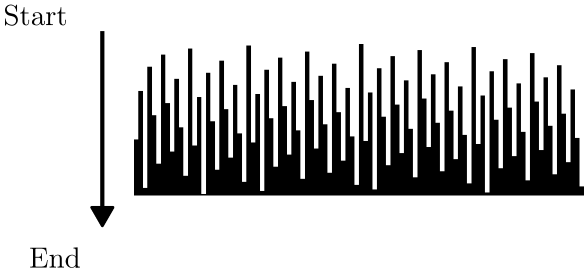

Figure 3: Visualization of iterative refinement algorithm. Black points show points already sampled. As can be seen we start at the top, knowing only a few points, converging on the full image in the end. This algorithm displays the general shape of a function earlier than its scanning counterpart. It can also be used for multidimensional parameter spaces

4 Results

Due to optimized sample geometry and effective implementation of the developed calibration tools and the resulting increase in SNR we present the to our knowledge first 2D ZULF experiment at natural abundance. We additionally developed a workflow to refine estimated J-coupling values using experimental spectra.

4.1 2D ZULF Spectroscopy at Natural Abundance

Disentangling complicated spectra is a problem, which is not unique to ZULF spectroscopy. Especially when looking at large molecules, such as during protein NMR, the large number of peaks can lead to overlap, hampering analysis. In 1975 Jean Jeener, Richard Ernst and coworkers attacked this problem by inventing 2D FFT NMR. The added dimension lead to a much sparser spectrum, allowing them to separate previously overlapping peaks. Nowadays 2D NMR has a wide range of applications within structural biology, drug discovery and more.[10] It is interesting to note, that some of the first ZULF spectra were two-dimensional, as they were prepared and detected at high field with a variable evolution at zero field, which allowed for indirect inferral of the ZULF spectrum.[31,32] However, the ZULF part of these spectra remained one-dimensional, as every data point in the ZULF dimension was a full experiment at HF. In this work we show directly detected 2d ZULF NMR at natural abundance. To our best knowledge this is the first time such spectra have been recorded. While others have shown 2D ZULF spectroscopy[33,34,13] before, they have always relied on the experimentally much more accessible ^{13}C labeled compounds. Moving to natural abundance compounds is both a big step towards applications within chemistry, where most compounds are unlabeled, as well as a door to cheaper and more elaborate ZULF experiments. Coupled with relaxed magnet requirements and novel operating regimes, this work seeks to progress ZULF NMR closer to real-world applications where the specificity of NMR is required, but its use is precluded due to cost, homogeneity, or throughput concerns.

ZFLF COSY

Zero Field Low Field Correlation SpectroscopY (ZFLF COSY) is a novel 2d spectrum, which combines evolution under the very complicated low field hamiltonian with the much simpler zero field Hamiltonian. The projection onto the direct dimension is exactly the ZF spectrum, while the projection onto the indirect dimension shows a LF spectrum. Cross peaks occur when there is a coherence transfer pathway between the ZF and LF states. The intensity is a measure of 'state overlap' (see SI B.2). Considering only very intense peaks we can find the 'fundamental building blocks' of the LF spectrum. For example, we can consider the single transition at ZF of a $^{13}C-H$ system. When moving to higher fields this single transition splits into three peaks, roughly centered around the original transition.[d] In this sequential picture it is clear that those side-peaks originate from the same J system. For simple systems this can also be seen by sweeping the B-field from ZULF to LF. If we consider the ZFLF spectrum of this system we see the single ZF peak in the direct dimension and the three peaks in the indirect dimension. Moreover, there are cross-peaks between the two peak clusters, indicating that they belong to the same spin group. For systems where the ZF spectrum is sparse there is no inherent advantage of the ZFLF spectrum as splitting can be assigned easily in the LF spectrum directly. However, when the spectrum becomes more complicated (for example when looking at mixtures of molecules with similar J values, or isotopic mixtures) the direct assignment becomes much more difficult.[9] The ZFLF spectrum however retains the easy interpretability so long as the peaks at ZF are well resolved and as long as the noise in the indirect dimension is sufficiently low. An additional use for the ZFLF spectrum is as a 'spectral ladder'. By performing ZFLF, LFMF (low field-medium field), MFHF (medium field-high field) spectra we should in theory be able to trace out the full coherence transfer pathway. We can now additionally connect information gained in other spectra such as the $5\mu T$ COSY proposed in.[13] The ZFLF concept can thus be used as a stepping stone between ZF and other NMR methods. For this work we performed ZFLF-COSY on methyl formate, at natural abundance. The result in figure 4 shows the expected projections onto the direct and indirect axes. It also highlights the peak separation, which is especially striking in the 250 Hz region. Due to the large variation in peak intensity some of the weaker peaks in our experiment cannot be resolved at the current moment. We believe that the next iteration of the experiment should have sufficient increases in SNR (we anticipate 4x-10x, which translates to 16x-100x in time). Pairing this with a longer acquisition time and non-uniform sampling should allow us to thus resolve all the minor peaks. As can be seen from figure 5 the real spectrum and the simulation are in qualitative agreement on the peaks that are resolved. There are some missing peaks, which can be explained by misalignment of the simulated detection axis and the experimental detection axis. This misalignment was willingly accepted for performance reasons. More specifically the first preparation part of the experiment was not simulated in detail, but instead replaced by an estimation of the prepared state. There is no in-principle reason why the simulation could not reproduce those peaks. The simulability of these spectra highlights another approach, where larger peaks can be used as alignment aid for the simulation, which then allows interpretation of the ULF spectrum via the simulation.

---

[d] Depending on the alignment of the polarization and detection axis these three peaks can simplify into only two peaks

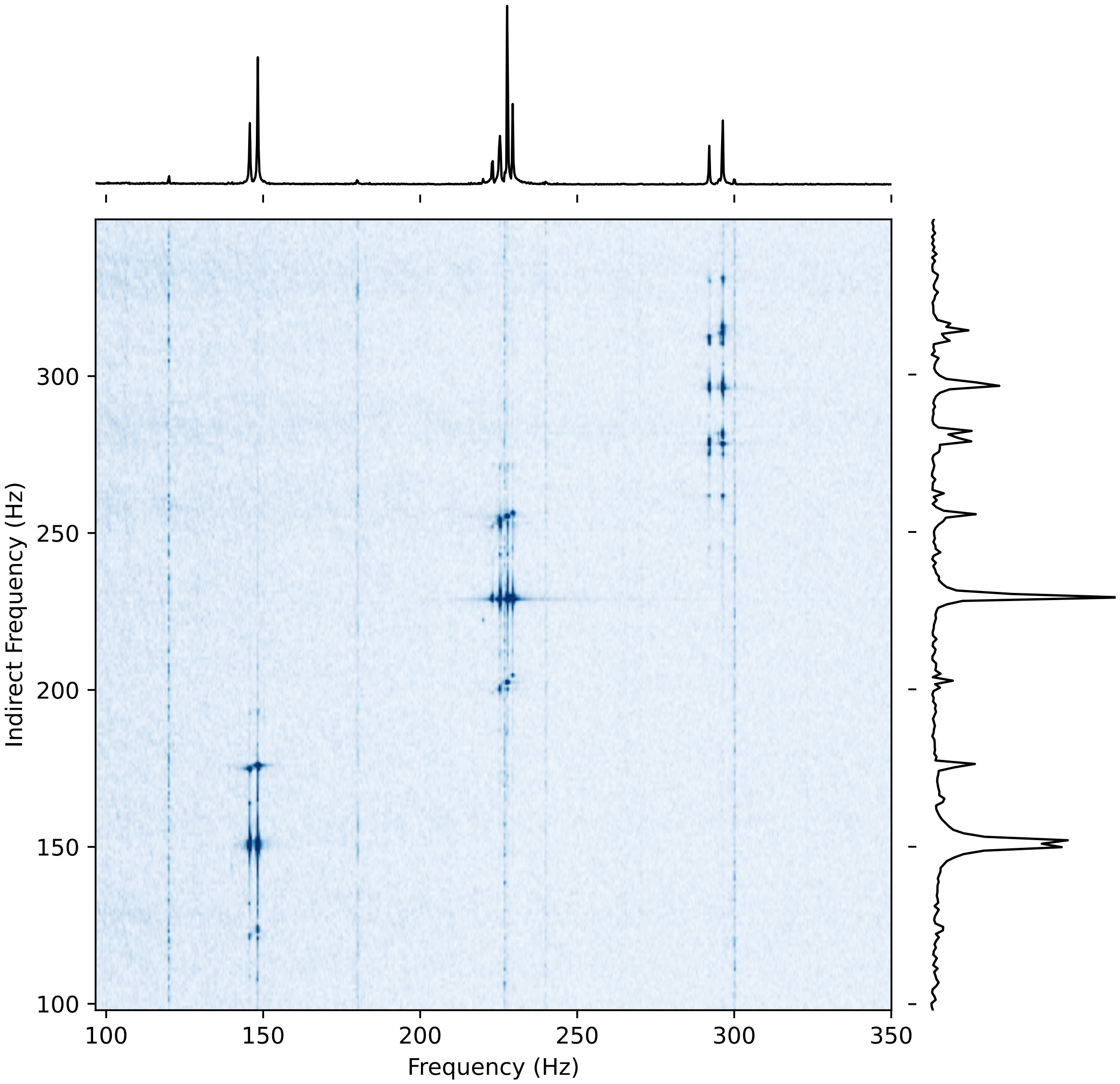

Figure 4: ZFLF COSY of methyl formate at natural abundance. The splitting in the indirect dimension gives information about the nature of the underlying spin system. Similarly, the separation in the direct ZF dimension allows for separation of overlapping peaks, especially in the 250Hz region. Environment peaks visible in the direct dimension are clearly separable from real peaks as they form vertical lines. The spectrum was baseline corrected in the direct dimension. No other adjustments, such as apodization were performed.

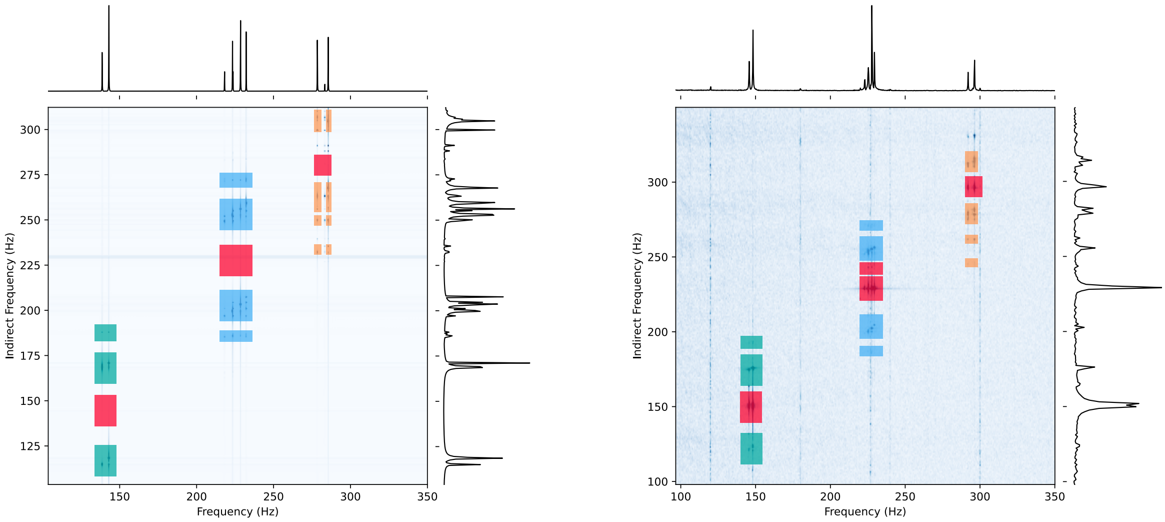

Figure 5: Comparison of simulated and real ZFLF COSY spectra. The simulation parameters were not specifically tuned to match experimental parameters. Agreement on the ZF axis is qualitatively given. Similar peak patterns were marked in blue and green. Related, but different patterns were marked in orange and differences were marked in red. On the LF axis there is a striking lack of central peaks in the simulation for each of the clusters. The authors attribute this to misalignment of the measurement axis between simulation and experiment. An additional difference can be seen for the 2J cluster of the methyl group. The ZF spectrum has a different intensity distribution between the three peaks in the simulation and the real experiment. The authors also attribute this difference to the axis misalignment.

True ZULF-COSY

True ZULF-COSY is conceptually closer to its high field equivalent. Whereas a classical COSY spectrum correlates high field spectra to themselves the ZULF-COSY works fully within the ZULF regime, meaning it correlates a ZULF spectrum to itself.

This leads to a symmetric spectrum, which displays cross peaks between peaks belonging to the same F manifold. In HF-COSY the cross peaks indicate a coupling between two hydrogens. In ZULF-COSY it indicates couplings between spin groups. This allows the spectrum to separate different compounds or isotopomers, which will not share the same F manifold.

To better understand the advantages of the method we can take a look at a simple model system XA_3B. To provide an easily understandable spectrum we chose the couplings to be as follows: $J_{XA} = 80Hz$ and $J_{XB} = 10Hz$. This is the same spin topology as formic acid with the label on the methyl-C. The ZULF spectrum produced for this molecule has been simulated using our custom software explained above. Relevant regions of absent peaks are labeled see figure 6. Further regions of potential interest are the low frequency components $< 10Hz$, which are often omitted from spectra for experimental reasons. The absence of cross peaks indicates that the spin systems in question are not connected. This can be due to selection rules such as F conservation, or because the spin systems are on different molecules. The second case commonly occurs in mixtures of isotopomers.

Equipped with the understanding of ZULF COSY we can now examine the experimental spectra. The following spectrum was captured on the aforementioned experimental spectrograph with a sample of methyl formate at natural abundance (see figure 7).

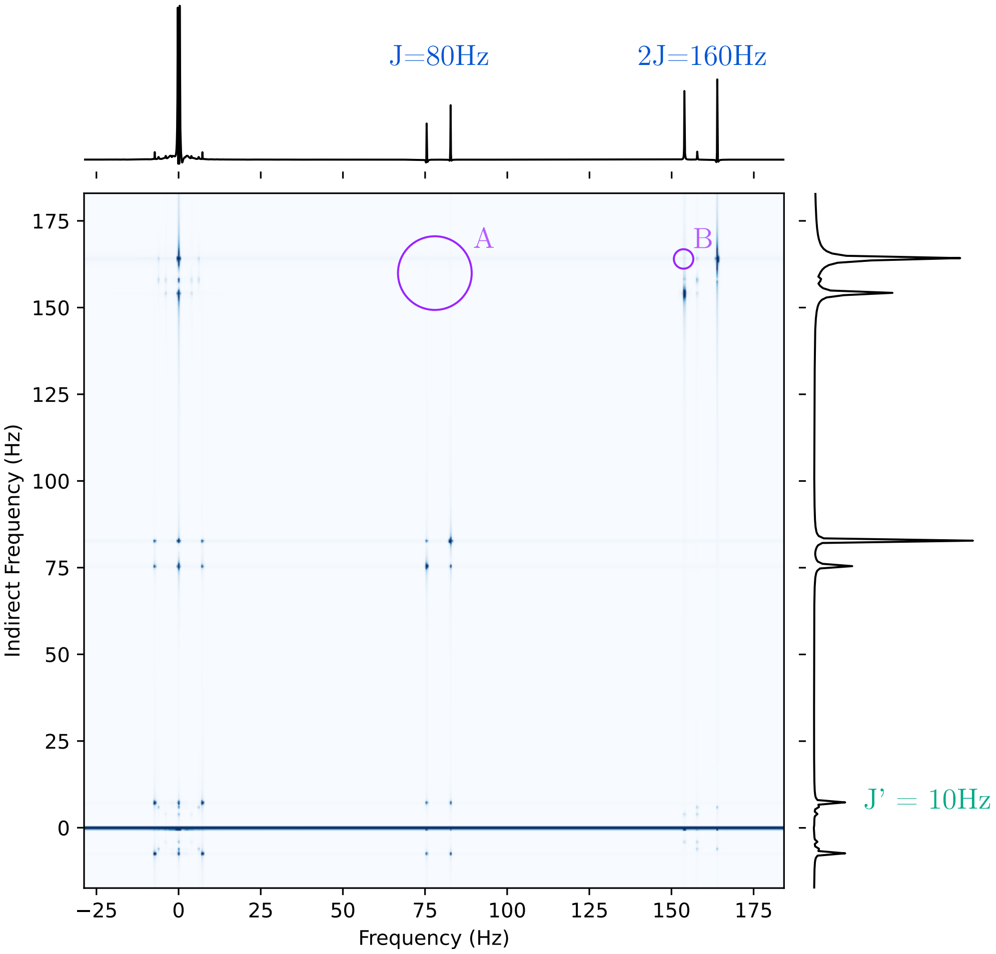

Figure 6: Simulated ZULF COSY spectrum of XA_3B system. As can be seen both dimensions show a classical ZULF spectrum. On the diagonal the expected peaks are visible. Cross peaks at (80,80) show connection within the $J = 80Hz$ system. Similarly, cross peaks at $2J = 160Hz$ are visible. Two regions of missing peaks A and B are marked in purple. The absence of the marked peaks allows for better characterization of the spin network. Absence A shows that the manifolds corresponding to the J and $2J$ peaks are independent of each other. For further discussion of the F structure within ZULF see.[35] The absence B shows that within the $2J$ peak-manifold there is no direct connection between the $|\uparrow\rangle_B$ perturbed and $|\downarrow\rangle_B$ perturbed peaks.

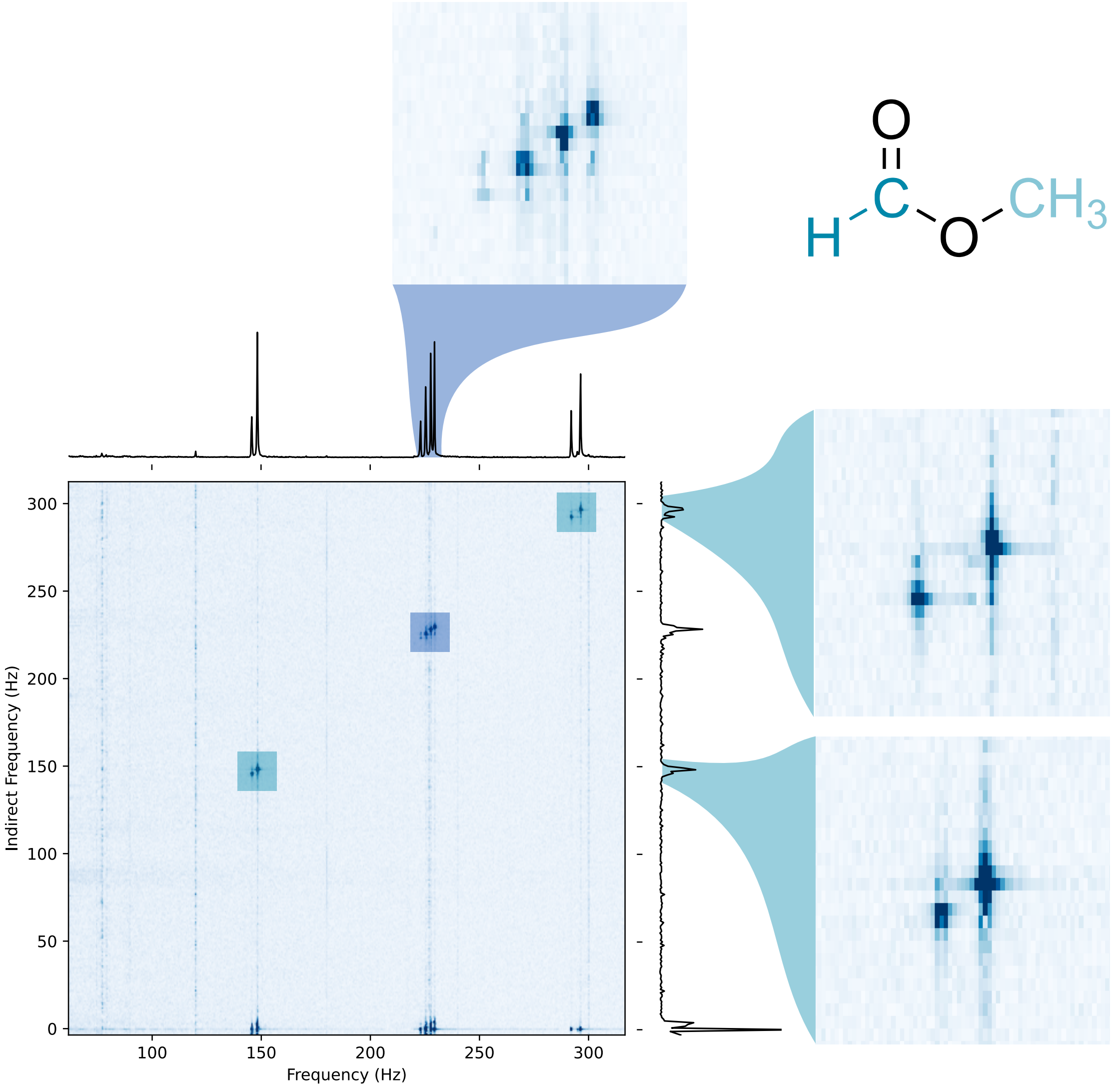

Figure 7: ZULF COSY spectrum of methyl formate at natural abundance. As can be seen there is an isotopic mixture of the methyl and formyl labeled compounds (marked in light and dark blue). The J and 2J structure of the methyl labeled part shows the rough peak shape seen in the simulated example in figure 6.

4.2 J extraction

Often the great complexity of ZULF spectra is mentioned as a fundamental drawback of ZULF. In this paper we propose a technique that allows us to reverse this inherent complexity to obtain the pure physical J coupling values. The technique is based on the local invertibility of differentiable functions. Using techniques from deep learning such as gradient based optimization we can leverage the simulability of our system to refine rough estimates of J coupling values. This has previously been done by Sjolander et al.[36] and by Bodensted.[37] Our method improves on the previous works by explicitly tying the simulation to the real experiment. This allows us to in-prinicple optimize for arbitrary experimental parameters, as well as compensate for custom state preparation. As a loss function the Wasserstein distance was chosen. To ensure physicality of the result the self coupling was forced to zero via l1 regularization. The derivative of the loss function was evaluated with respect to the J values used for the simulation. This was done via back-propagation, which was possible due to the differentiable nature of our simulation. This back-propagated loss was then optimized using the Adam optimizer[38] and an additional annealing term, which enforces convergence. For additional details readers are referred to the open source codebase.[39]

Our scheme was tested by trying to reconstruct simulated spectra. For this purpose a sample of $N = 100$ initially perturbed methyl formate molecules was used as an initial guess. The optimization algorithm was run for 300 steps. The resulting J values were clustered into converged and non converged according to the loss function in the last iteration of the cycle. The converged samples were used to reconstruct the J matrix (see figure 9)

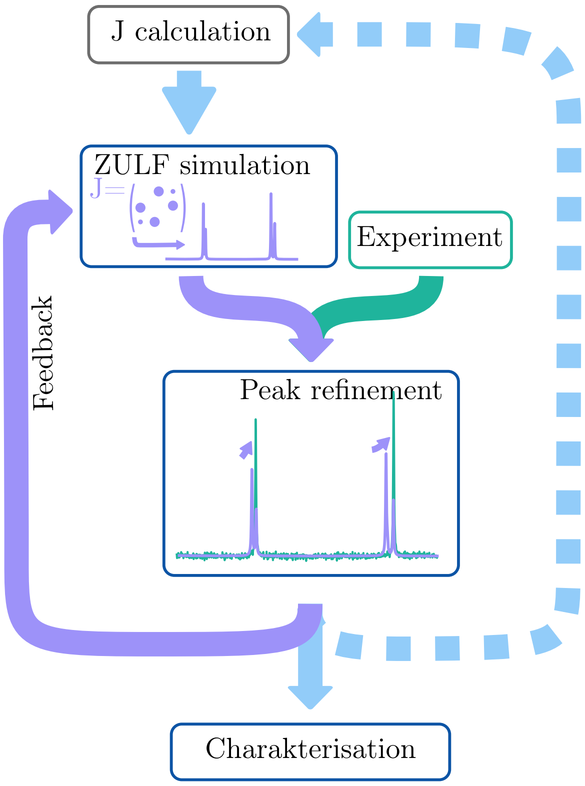

Figure 8: Schematic overview of the interplay between experimental data, simulations, and the refinement algorithm. An initial guess can be calculated via *ab initio* methods such as DFT. This guess is then used to simulate ZULF spectra. Those spectra are then compared with experimental data to obtain error-gradients, which are then used to tune simulation parameters. This cycle is repeated until the desired accuracy is reached. The underlying J-coupling values can now be extracted and used for characterization of the spin systems. They can also be used to compare with the initial *ab initio* guess.

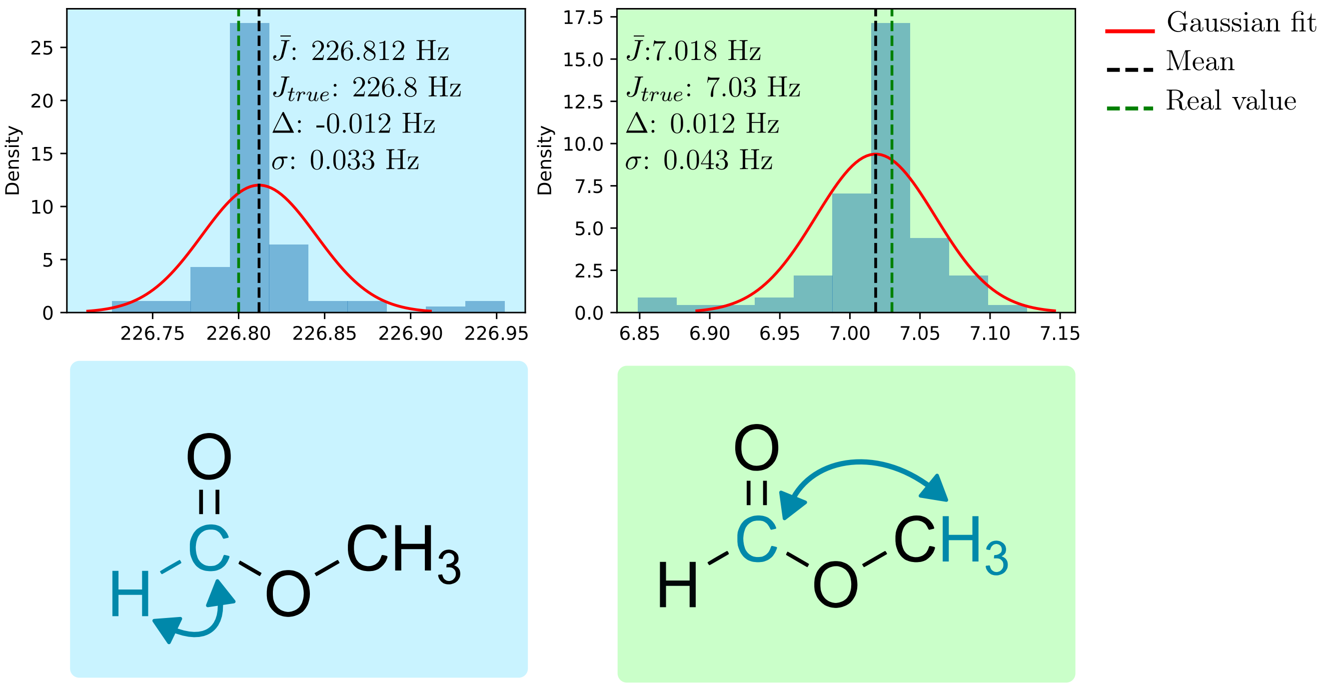

Figure 9: Convergence stability for formyl labeled methyl formate as measured against simulated data. $N = 100$ samples with $J_{sample} = (1 + \delta) \cdot J_{true}$ were used as starting point for the convergence algorithm with $\delta = 5\%$. The convergence algorithm was run for 300 steps on the Euler HPC cluster. The final results were clustered into successful and unsuccessful convergence. All data shown herein is picked from the set of successful convergences. The algorithm shows promising convergence accuracy for small molecules. It is known that larger molecules will present difficulties for this algorithm, as perturbations in the large couplings will strongly influence overlap in low frequency i.e., small coupling regions. For ways to alleviate these anticipated issues see the discussion section of this paper 5

5 Outlook

In this work we have shown substantial improvements in ZULF sensitivity, which was used to perform a variety of so-far inaccessible experiments. This paper shows the to our knowledge first ZULF-COSY and ZFLF-COSY experiments at natural abundance. We also prototype a workflow for reconstructing J-coupling values from experimental spectra via a differentiable simulation. Further improvements in sensitivity could lead to better resolved 2D ZULF experiments at natural abundance, which paves the way towards applying 2D ZULF in more contexts, such as kinetic studies of liquids in porous media. The refinement scheme has been demonstrated to work on small molecules. The authors believe that modifying the convergence algorithm to first optimize the large couplings and then work on the details would allow them to scale the method to larger systems. Alternative approaches such as simulated annealing could also lead to better J predictions. Future work should explore the quantitative relations between molecule complexity, SNR and convergence probability as well as convergence accuracy.

This paper has shown the promise of using computer modeling for experiment design and optimization and has leveraged the improved understanding and easy operation of the setup to design novel experiments. Using the techniques developed in this work we hope that future projects can similarly be optimized and understood.

References

[1] Angela M. Gronenborn and Tatyana Polenova. "Introduction: Biomolecular NMR Spectroscopy". In: *Chemical Reviews* 122.10 (May 2022), pp. 9265–9266. ISSN: 0009-2665. DOI: `10.1021/acs.chemrev.2c00142`. (Visited on 05/19/2025).

[2] M. E. Smith and J. H. Strange. "NMR Techniques in Materials Physics: A Review". In: *Measurement Science and Technology* 7.4 (Apr. 1996), p. 449. ISSN: 0957-0233. DOI: `10.1088/0957-0233/7/4/002`. (Visited on 05/19/2025).

[3] Boaz Shapira and Lucio Frydman. "Spatial Encoding and the Acquisition of High-Resolution NMR Spectra in Inhomogeneous Magnetic Fields". In: *Journal of the American Chemical Society* 126.23 (June 2004), pp. 7184–7185. ISSN: 0002-7863. DOI: `10.1021/ja048859u`. (Visited on 03/20/2025).

[4] Blake Andrews et al. *High-Sensitivity Multichannel Zero-to-Ultralow Field NMR with Atomic Magnetometer Arrays*. June 2024. DOI: `10.48550/arXiv.2407.00929`. arXiv: `2407.00929 [physics]`. (Visited on 09/14/2024).

[5] David J. Griffiths. *Introduction to Electrodynamics*. Fifth edition. New York: Cambridge University Press, 2023. ISBN: 978-1-009-39775-9.

[6] Dudari B. Burueva et al. "Chemical Reaction Monitoring Using Zero-Field Nuclear Magnetic Resonance Enables Study of Heterogeneous Samples in Metal Containers". In: *Angewandte Chemie International Edition* 59.39 (2020), pp. 17026–17032. ISSN: 1521-3773. DOI: `10.1002/anie.202006266`. (Visited on 03/20/2025).

[7] Michael C. D. Tayler, Jordan Ward-Williams, and Lynn F. Gladden. "NMR Relaxation in Porous Materials at Zero and Ultralow Magnetic Fields". In: *Journal of Magnetic Resonance* 297 (Dec. 2018), pp. 1–8. ISSN: 1090-7807. DOI: `10.1016/j.jmr.2018.09.014`. (Visited on 07/17/2025).

[8] Dudari B. Burueva et al. *Chemical Reaction Monitoring Using Zero-Field Nuclear Magnetic Resonance Enables Study of Heterogeneous Samples in Metal Containers*. Apr. 2020. DOI: `10.26434/chemrxiv.12168312.v1`. (Visited on 07/22/2025).

[9] S. Appelt et al. "Paths from Weak to Strong Coupling in NMR". In: *Physical Review A* 81.2 (Feb. 2010), p. 023420. ISSN: 1050-2947, 1094-1622. DOI: `10.1103/PhysRevA.81.023420`. (Visited on 10/04/2024).

[10] Richard R. Ernst et al. *Principles of Nuclear Magnetic Resonance in One and Two Dimensions*. International Series of Monographs on Chemistry. Oxford, New York: Oxford University Press, May 1990. ISBN: 978-0-19-855647-3.

[11] *The Nobel Prize in Chemistry 1991*. https://www.nobelprize.org/prizes/chemistry/1991/9148-two-dimensional-nmr/. (Visited on 07/08/2025).

[12] Chris Schaller. *COSY Spectra - LibreTexts*. Oct. 2022.

[13] Jeong Hyun Shim et al. "Two-Dimensional NMR Spectroscopy of 13C Methanol at Less than $5 \mu T$". In: *Journal of Magnetic Resonance* 246 (Sept. 2014), pp. 4–8. ISSN: 1090-7807. DOI: `10.1016/j.jmr.2014.06.018`. (Visited on 03/04/2025).

[14] David E. Rumelhart, Geoffrey E. Hinton, and Ronald J. Williams. "Learning Representations by Back-Propagating Errors". In: *Nature* 323.6088 (Oct. 1986), pp. 533–536. ISSN: 1476-4687. DOI: `10.1038/323533a0`. (Visited on 05/19/2025).

[15] *SDBS NMR Database*.

[16] James J. Keeler. *Understanding NMR Spectroscopy.* 2. ed., repr. Chichester: Wiley, 2011. ISBN: 978-0-470-74608-0 978-1-119-96493-3.

[17] *Twinleaf — MS-2.* https://twinleaf.com/shield/MS-2/. (Visited on 07/22/2025).

[18] *QZFM Gen-3 – QuSpin.* https://quspin.com/products-qzfm/. (Visited on 07/22/2025).

[19] *PyQt5: Python Bindings for the Qt Cross Platform Application Toolkit.*

[20] Charles R. Harris et al. "Array Programming with NumPy". In: *Nature* 585.7825 (Sept. 2020), pp. 357–362. DOI: `10.1038/s41586-020-2649-2`.

[21] Pauli Virtanen et al. "SciPy 1.0: Fundamental Algorithms for Scientific Computing in Python". In: *Nature Methods* 17.3 (Mar. 2020), pp. 261–272. ISSN: 1548-7105. DOI: `10.1038/s41592-019-0686-2`. (Visited on 05/19/2025).

[22] J. R. Johansson, P. D. Nation, and Franco Nori. "QuTiP: An Open-Source Python Framework for the Dynamics of Open Quantum Systems". In: *Computer Physics Communications* 183.8 (Aug. 2012), pp. 1760–1772. ISSN: 0010-4655. DOI: `10.1016/j.cpc.2012.02.021`. (Visited on 03/15/2025).

[23] *HIPS/Autograd.* Formerly: Harvard Intelligent Probabilistic Systems Group – Now at Princeton. Mar. 2025. (Visited on 03/11/2025).

[24] *Ajoy-Lab/ZULFPy: Repository of Python Code for the ZULF Setup in the Ajoy Lab @ Berkeley.* https://github.com/Ajoy-Lab/ZULFPy. (Visited on 03/15/2025).

[25] Brian E. Granger and Fernando Pérez. "Jupyter: Thinking and Storytelling With Code and Data". In: *Computing in Science & Engineering* 23.2 (Mar. 2021), pp. 7–14. ISSN: 1558-366X. DOI: `10.1109/MCSE.2021.3059263`. (Visited on 03/15/2025).

[26] *JupyterHub - ScientificComputing.* https://scicomp.ethz.ch/wiki/JupyterHub. (Visited on 05/19/2025).

[27] Neill Lambert et al. *QuTiP 5: The Quantum Toolbox in Python.* Dec. 2024. DOI: `10.48550/arXiv.2412.04705`. arXiv: `2412.04705 [quant-ph]`. (Visited on 03/15/2025).

[28] J.R. Johansson, P.D. Nation, and F. Nori. "QuTiP 2: A Python Framework for the Dynamics of Open Quantum Systems". In: *Computer Physics Communications* 184.4 (Apr. 2013), pp. 1234–1240. DOI: `10.1016/j.cpc.2012.11.019`.

[29] J.R. Johansson, P.D. Nation, and F. Nori. "QuTiP: An Open-Source Python Framework for the Dynamics of Open Quantum Systems". In: *Computer Physics Communications* 183.8 (Aug. 2012), pp. 1760–1772. DOI: `10.1016/j.cpc.2012.02.021`.

[30] John W. Blanchard et al. "High-Resolution Zero-Field NMR J-Spectroscopy of Aromatic Compounds". In: *Journal of the American Chemical Society* 135.9 (Mar. 2013), pp. 3607–3612. ISSN: 0002-7863. DOI: `10.1021/ja312239v`. (Visited on 10/07/2024).

[31] D. P. Weitekamp et al. "Zero-Field Nuclear Magnetic Resonance". In: *Physical Review Letters* 50.22 (May 1983), pp. 1807–1810. DOI: `10.1103/PhysRevLett.50.1807`. (Visited on 03/19/2025).

[32] Ann M. Thayer and Alexander Pines. "Zero-Field NMR". In: *Accounts of Chemical Research* 20.2 (Feb. 1987), pp. 47–53. ISSN: 0001-4842. DOI: `10.1021/ar00134a001`. (Visited on 03/19/2025).

[33] Tobias F. Sjolander et al. "Two-Dimensional Single- and Multiple-Quantum Correlation Spectroscopy in Zero-Field Nuclear Magnetic Resonance". In: *Journal of Magnetic Resonance* 318 (Sept. 2020), p. 106781. ISSN: 1090-7807. DOI: `10.1016/j.jmr.2020.106781`. (Visited on 03/03/2025).

[34] Seong-Joo Lee et al. "Chemical Analysis of an Isotopically Labeled Molecule Using Two-Dimensional NMR Spectroscopy at $34 \mu T$". In: *ACS Omega* 8.40 (Oct. 2023), pp. 37302–37308. DOI: `10.1021/acsomega.3c05128`. (Visited on 03/03/2025).

[35] John Woodland Blanchard. “Zero and Ultra-Low-Field Nuclear Magnetic Resonance Spectroscopy Via Optical Magnetometry”. In: ().

[36] Tobias F. Sjolander et al. “13C-Decoupled J-Coupling Spectroscopy Using Two-Dimensional Nuclear Magnetic Resonance at Zero-Field”. In: *The Journal of Physical Chemistry Letters* 8.7 (Apr. 2017), pp. 1512–1516. DOI: `10.1021/acs.jpclett.7b00349`. (Visited on 07/22/2025).

[37] Sven Bodenstedt. “Optically Detected Nuclear Magnetic Resonance above and Far below Earth’s Magnetic Field: Spin Dynamics and Relaxation in Unconventional Regimes”. PhD thesis. Universitat Politècnica de Catalunya, Feb. 2024. DOI: `10.5821/dissertation-2117-406472`. HDL: `2117/406472`. (Visited on 07/22/2025).

[38] Diederik P. Kingma and Jimmy Ba. *Adam: A Method for Stochastic Optimization.* Jan. 2017. DOI: `10.48550/arXiv.1412.6980`. arXiv: `1412.6980 [cs]`. (Visited on 07/17/2025).

[39] *Ajoy-Lab/ZULFPy: Repository of Python Code for the ZULF Setup in the Ajoy Lab @ Berkeley.* https://github.com/Ajoy-Lab/ZULFPy. (Visited on 07/22/2025).

Acknowledgment

I would like to thank my advisor Blake Andrews for giving me the necessary creative space to develop some of my ideas independently, while still giving me the guidance I needed to get started in the project, as well as proofreading the first draft of this thesis. I would also like to thank the entire Ajoy Lab for providing a helpful and productive environment. Additionally I would like to thank Prof. Ashok Ajoy and Prof. Alexander Barnes for giving me this great oportunity.

Lastly I want to thank my friends and familiy for always standing by my side and helping me stay motivated.

A Declaration of Originality

The text of this manuscript was written without the help of generative AI. To speed up the workflow during creation of the simulations the genAI tool GitHub Copilot was used for code completion. The author takes full responsibility for the form and content of the code. Both architectural as well as algorithmic decisions were taken by the author themselves.

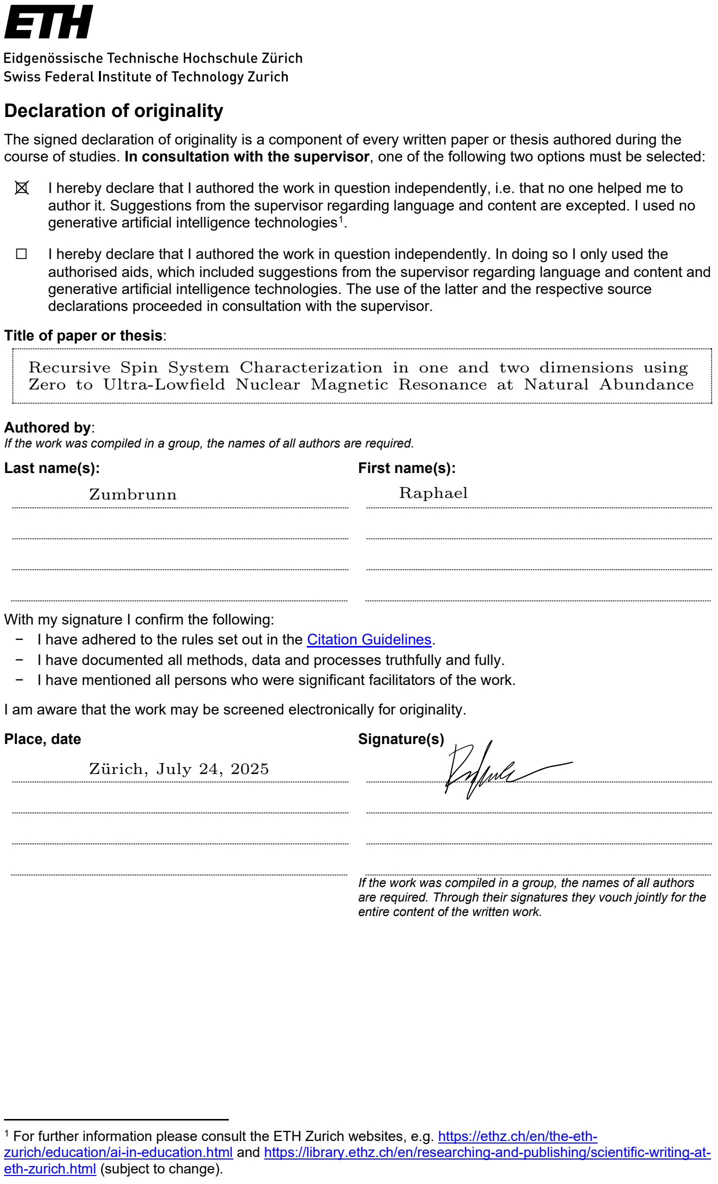

Eidgenössische Technische Hochschule Zürich
Swiss Federal Institute of Technology Zurich

Declaration of originality

The signed declaration of originality is a component of every written paper or thesis authored during the course of studies. **In consultation with the supervisor**, one of the following two options must be selected:

☒ I hereby declare that I authored the work in question independently, i.e. that no one helped me to author it. Suggestions from the supervisor regarding language and content are excepted. I used no generative artificial intelligence technologies[1].

☐ I hereby declare that I authored the work in question independently. In doing so I only used the authorised aids, which included suggestions from the supervisor regarding language and content and generative artificial intelligence technologies. The use of the latter and the respective source declarations proceeded in consultation with the supervisor.

Title of paper or thesis:

Recursive Spin System Characterization in one and two dimensions using Zero to Ultra-Lowfield Nuclear Magnetic Resonance at Natural Abundance

Authored by:
If the work was compiled in a group, the names of all authors are required.

Last name(s):	**First name(s):**
Zumbrunn	Raphael

With my signature I confirm the following:

- I have adhered to the rules set out in the Citation Guidelines.
- I have documented all methods, data and processes truthfully and fully.
- I have mentioned all persons who were significant facilitators of the work.

I am aware that the work may be screened electronically for originality.

Place, date	**Signature(s)**
Zürich, July 24, 2025	

If the work was compiled in a group, the names of all authors are required. Through their signatures they vouch jointly for the entire content of the written work.

---

[1] For further information please consult the ETH Zurich websites, e.g. https://ethz.ch/en/the-eth-zurich/education/ai-in-education.html and https://library.ethz.ch/en/researching-and-publishing/scientific-writing-at-eth-zurich.html (subject to change).

B Supporting Information

B.1 Additional work

This part is a non-comprehensive overview of work performed in the course of my bachelor thesis, which was not deemed relevant enough for the main part of this thesis. It also contains partially finished work, which might be developed further in future projects.

Temperature regulation PCB

It has been shown that temperature can influence effective J couplings, as observed at ZULF. To quantify and potentially mitigate broadening due to temperature drift a PCB was designed with the purpose of stabilizing a given temperature within the sample. Due to spatial constraints a custom PCB was developed around the NTCLE100E3102HB0 thermistor. The PCB uses a negative feedback scheme via the operational amplifier MCP6487T-E/SN, that heats a sample according to a temperature set resistor.

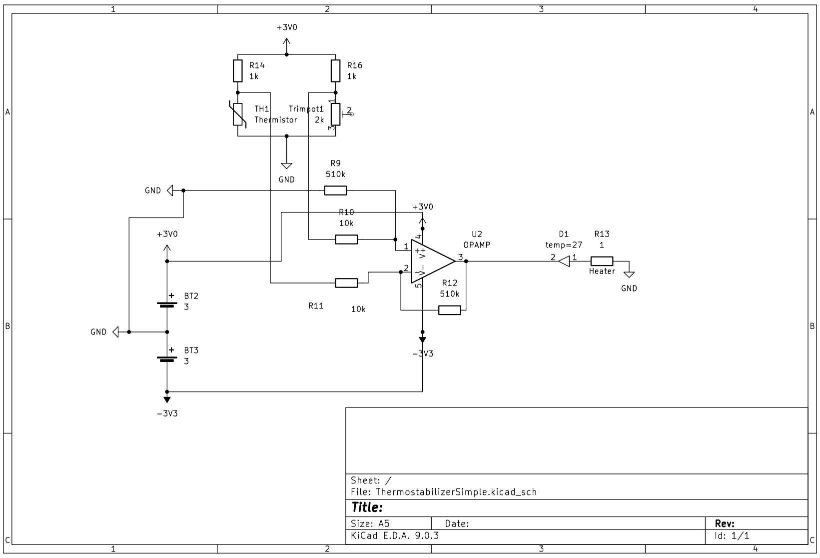

Figure 10: Schematic of the feedback-controlled thermal regulator. The circuit is built from wheatstone-bride, translating the resistance into a voltage, an operational amplifier in the negative feedback regime and a heater connected to a diode. The diode is necessary because we can only heat, but cannot cool the system using the coil.

The PCB has been simulated in KiCad and shows the desired linear feedback response it was designed for. Due to temporal restrictions on the project, as well as difficulties in delivery of custom PCBs testing of the real circuit was not yet performed.

Micro Saddle Coil fabrication

For a seperate project a novel method to template and build micro saddle coils $\varnothing 3mm$ was prototyped. Solubility experiments with a range of solvents was performed on standard 3D printer PLA (Poly lactic acid) filament. A technique involving a combination of DCM (Dichloromethane) and Ethanol was developed. The procedure can be summarized as follows:

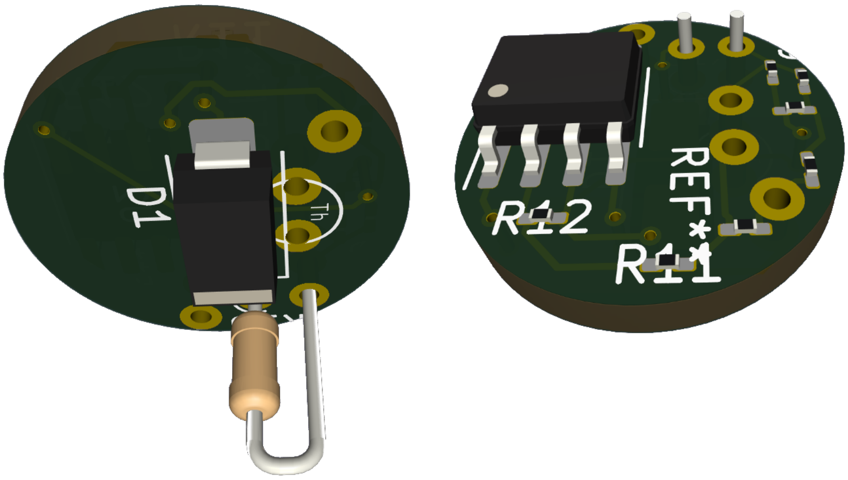

Figure 11: 3D render of thermal regulation PCB as seen from the bottom (left) and the top (right). The large reistor seen from the bottom is used for heating and can be submerged in the sample if necessary. The largest design hurdle for this PCB was the small footprint (12.25mm ∅)

1. 3D print scaffolding for saddle coil
2. Wrap coil around scaffold
3. Put coil & scaffold container filled with 50:50 (vol) DCM and Ethanol
4. PLA will dissolve in DCM, ethanol provides momentum to remove it from DCM

B.2 Mathematical derivations

Diagonal solver

We start from the known solution to the Liouvile-Von-Neumann equation to stationary hamiltonians iii, which we can simplify by diagonalizing $\hat{H}$. We will call the new Hamiltonian in its own energy eigenbasis $\hat{E}$.

$$\rho(t) = \exp\left(\frac{1}{i\hbar}\hat{H}t\right)\rho_0 \exp\left(-\frac{1}{i\hbar}\hat{H}t\right) \tag{iii}$$

$$= \exp\left(\frac{1}{i\hbar}U^{-1}\hat{E}tU\right)\rho_0 \exp\left(-\frac{1}{i\hbar}U^{-1}\hat{E}tU\right) \tag{iv}$$

We now want to calculate the expectation value of some observable such as the magnetisation $\hat{M}$. For this we can use the trace formula v. Which we expand and then use the cyclicity of the trace to obtain vii

$$
\begin{aligned}
\langle M\rangle(t) &= \operatorname{tr}\Big(\hat{M}\rho(t)\Big) && \text{(v)}\\
&= \operatorname{tr}\left(\hat{M}\exp\left(\frac{1}{i\hbar}U^{-1}\hat{E}tU\right)\rho_0\exp\left(-\frac{1}{i\hbar}U^{-1}\hat{E}tU\right)\right) && \text{(vi)}\\
&= \operatorname{tr}\left(U\hat{M}U^{-1}\exp\left(\frac{1}{i\hbar}\hat{E}t\right)U\rho_0U^{-1}\exp\left(-\frac{1}{i\hbar}\hat{E}t\right)\right) && \text{(vii)}\\
&= \operatorname{tr}\left(\hat{M}_E\exp\left(\frac{1}{i\hbar}\hat{E}t\right)\rho_{0E}\exp\left(-\frac{1}{i\hbar}\hat{E}t\right)\right) && \text{(viii)}
\end{aligned}
$$

We can rewrite $U\hat{M}U^{-1}$ and $Urho_0U^{-1}$ by realizing this is simply a basis transformation into the energy eigenbasis as $\hat{U}_E$ and ρ_{0E}. This form is convenient, as it allows us to transform the expensive matrix exponential into the exponential of a diagonal matrix, which is very simple. Additionally the time dependent part is now easy to compute.

To obtain a formula in the frequency domain we now apply the fourier transform.

$$
\begin{aligned}
\langle M\rangle(\omega) &= \int_{-\infty}^{\infty}\langle M\rangle(t)\exp(i\omega t)dt && \text{(ix)}\\
&= \int_{-\infty}^{\infty}\operatorname{tr}(\ldots)dt && \text{(x)}\\
&= \operatorname{tr}\left(\int_{-\infty}^{\infty}\ldots dt\right) && \text{(xi)}\\
&= \operatorname{tr}\left(\int_{-\infty}^{\infty}(\hat{M}_{E,i,k}\exp\left(\frac{1}{i\hbar}E_kt\right)\rho_{0E,k,j}\exp\left(-\frac{1}{i\hbar}E_jt\right)\exp(i\omega t))_{i,j}\right) && \text{(xii)}\\
&= \operatorname{tr}\left(\int_{-\infty}^{\infty}(\hat{M}_{E,i,k}\rho_{0E,k,j}\exp\left(it(\omega-\frac{1}{\hbar}(E_k-E_j))\right))_{i,j}\right) && \text{(xiii)}\\
&= \operatorname{tr}\left((\hat{M}_{E,i,k}\rho_{0E,k,j}\delta\left(\omega-\frac{1}{\hbar}(E_k-E_j)\right))_{i,j}\right) && \text{(xiv)}
\end{aligned}
$$

From expression xiv we realize that the only ω where a matrix element can be non-zero are those which fulfill $\omega = \frac{1}{i\hbar}\Delta E$. Thus the only observable transitions are those at frequencies which match a difference between energy levels. This formula also suggests a straight forward way to compute a spectrum.

1. Diagonalize Hamiltonian to obtain U
2. Transform observables and states to energy eigenbasis
3. For every pair of energylevels compute formula xiv

The result will be a list of peak positions and amplitudes, which can be easily transformed into a spectrum.

There are three main advantages to this specific implementation of a solver:

- Fast, can take advantage of DFT matrix multiplication and GPU acceleration.
- Locally differentiable, can be used for backpropagation
- Cheap to paralellize, can calculate multiple observables at minimal overhead.

ZFLF COSY

Zero Field Low Field Correlation SpectroscopY can be mathematically described as a sequence of evolutions under partially overlapping hamiltonians $\bar{H}_{ZF}$ and $\bar{H}_{LF}$. The sequence for the experiment is as follows:

$$\rho_0 \xrightarrow[\tau]{\hat{H}_{LF}} \rho_1 \xrightarrow[t]{\hat{H}_{ZF}} \rho_2 \tag{xv}$$

The variable τ can be varied over multiple experiments, ρ_2 will be aquired for many values of t per experiment according to the temporal resolution of detection and detection time T.

We can observe how ρ_2 depends on the two parameters t, τ.

$$\begin{aligned}
\rho_2 &= \hat{U}_{ZF}(t)\rho_1\hat{U}^{-1}_{ZF}(t) && \text{(xvi)}\\
&= \hat{U}_{ZF}(t)\hat{U}_{LF}(\tau)\rho_0\hat{U}^{-1}_{LF}(\tau)\hat{U}^{-1}_{ZF}(t) && \text{(xvii)}\\
&= \exp\left(\frac{1}{i\hbar}\hat{H}_{LF}\tau\right)\exp\left(\frac{1}{i\hbar}\hat{H}_{ZF}t\right)\cdot\rho_0\cdot\text{h.c.} && \text{(xviii)}
\end{aligned}$$

We write the matrix elements explicitly using einstein-summation. We also use the fact that the hamiltonians are diagonalizable. We can then take the eigenvectors out of the exponential xx by the exponation of diagonal matrices formula.

$$\begin{aligned}
\rho^2_{i,l} &= \exp\left(\frac{1}{i\hbar}E_i^{LF}\,|i^{LF}\rangle\langle i^{LF}|\,\tau\right)\exp\left(\frac{1}{i\hbar}E_j^{ZF}\,|j^{ZF}\rangle\langle j^{ZF}|\,t\right)\cdot\rho_0\cdot\text{h.c.} && \text{(xix)}\\
&= \exp\left(\frac{1}{i\hbar}(E_i^{LF}\tau + E_j^{ZF}t)\right)|i^{LF}\rangle\langle i^{LF}|\,|j^{ZF}\rangle\langle j^{ZF}|\cdot|\rho_j^0\rangle\langle\rho_k^0|\cdot\text{h.c} && \text{(xx)}\\
&= \overbrace{\exp\left(\frac{1}{i\hbar}((E_i^{LF}-E_l^{LF})\tau + (E_j^{ZF}-E_k^{ZF})t)\right)}^{A}\cdot && \text{(xxi)}\\
&\underbrace{|i^{LF}\rangle\langle i^{LF}|\,|j^{ZF}\rangle\langle j^{ZF}|\,|\rho_j^0\rangle\langle\rho_k^0|\,|k^{ZF}\rangle\langle k^{ZF}|\,|l^{LF}\rangle\langle l^{LF}|}_{B} && \text{(xxii)}\\
& && \text{(xxiii)}
\end{aligned}$$

We now obtain a two part expression. Part A contains all the energy and time components and takes the form of a scalar. Part B is more complicated and takes the form of a projector, which we will analyze further in the next parts.
The reason why this decomposition is usefull can be directly seen when we apply the fourier transform. The separation of scalar-valued functions of t and τ from the more complicated operator allows straight forward evaluation of the fourier transform.

$$\rho^2_{i,j}(\omega,\tilde{\omega}) = \underbrace{\delta(\frac{1}{\hbar}(E_i^{LF}-E_l^{LF}-\tilde{\omega}))\delta(\frac{1}{\hbar}(E_j^{ZF}-E_k^{ZF}-\omega))}_{\tilde{A}}\cdot B \tag{xxiv}$$

We directly obtain the selection rules for ZFLF, which turn out to be the same as for ZF and LF respectiveley along their dimensions[e].

In fact $\tilde{A}$ acts as to pick out pairs of eigenstates (read transitions) at ZF and LF indexed by ω and $\tilde{\omega}$. It is of interest now to see what happens to the intensity of those allowed transitions. To make our calculations easier we will first look at only the intensity of eigenstate-pairs, which can then be

---

[e] Energy difference must match the peak frequency

summed up over degenerate transitions. As we eventually care about the observable magnetisation $\langle M\rangle$ we will consider $tr(M\rho)$. Consider first that the pair of i and l is fixed.

$$\begin{aligned}
\langle M\rangle(\omega,\tilde{\omega}) &= tr(\tilde{A}\overbrace{\left|i^{LF}\right\rangle\!\left\langle i^{LF}\right| \left|j^{ZF}\right\rangle\!\left\langle j^{ZF}\right| \left|\rho_j^0\right\rangle\!\left\langle\rho_k^0\right| \left|k^{ZF}\right\rangle\!\left\langle k^{ZF}\right| \left|l^{LF}\right\rangle\!\left\langle l^{LF}\right|}^{B} M) \tag{xxv}\\
&= \sum_h \left\langle h^{LF}\right| \tilde{A} \left|i^{LF}\right\rangle\!\left\langle i^{LF}\right| \left|j^{ZF}\right\rangle\!\left\langle j^{ZF}\right| \left|\rho_j^0\right\rangle\!\left\langle\rho_k^0\right| \left|k^{ZF}\right\rangle\!\left\langle k^{ZF}\right| \left|l^{LF}\right\rangle\!\left\langle l^{LF}\right| M \left|h^{LF}\right\rangle \tag{xxvi}\\
&= \tilde{A}\left\langle i^{LF}\right| \left|j^{ZF}\right\rangle\!\left\langle j^{ZF}\right| \left|\rho_j^0\right\rangle\!\left\langle\rho_k^0\right| \left|k^{ZF}\right\rangle\!\left\langle k^{ZF}\right| \left|l^{LF}\right\rangle\!\left\langle l^{LF}\right| M \left|i^{LF}\right\rangle \tag{xxvii}
\end{aligned}$$

We now define the projected states $\left|i^{LF}\right\rangle_j = \left|j^{ZF}\right\rangle\left\langle j^{ZF}\middle|i^{LF}\right\rangle$. Note this is a ZF state, with amplitude proportional to the overlap of i and j.

$$\langle M\rangle(\omega,\tilde{\omega}) = \tilde{A}\underbrace{\left\langle i_j^{LF}\right| \left|\rho_j^0\right\rangle\!\left\langle\rho_k^0\right| \left|l_k^{LF}\right\rangle}_{D}\underbrace{\left\langle l^{LF}\right| M \left|i^{LF}\right\rangle}_{E} \tag{xxviii}$$

Because we decided previously that l and i would be fixed we now have straightforwardly interpretable formula. Part E represents the standard LF amplitude for the selected transition. This will remain the same for any of the peaks along the ω dimension. It is from this part of the formula that we can also derive that the projection of the ZFLF spectrum onto any of the two axes will be the same as a 1D spectrum along this axis[f]. The more interesting part of this equation is part D. We can see from this that the modulation between ZF peaks for the same selected LF peak is an indicator of "transition-overlap". It essentially shows how much each ZF peak contributes to the LF peak.

The mathematical findings of this paragraph are also exemplified by our experimental data, where we see spectrum follow these exact selection rules. For an alternative treatment of general 2D experiments using superoperators the reader is refered to.[10]

ZULF COSY

The derivation of the amplitudes ZFLF COSY can be directly transformed to ZULF COSY by letting $B \to 0$. By changing the low field energies to the zero field energies in eq. xxiv we obtain:

$$\rho^2_{i,j}(\omega,\tilde{\omega}) = \underbrace{\delta(\frac{1}{\hbar}(E_i^{ZF} - E_l^{ZF} - \tilde{\omega}))\delta(\frac{1}{\hbar}(E_j^{ZF} - E_k^{ZF} - \omega))}_{\tilde{A}^{COSY}} \cdot B^{COSY} \tag{xxix}$$

This directly shows that the projection onto both the direct and indirect axis are equivalent to a standard 1D ZULF experiment. Evaluating B^{COSY} we can follow the same procedure as outlined in B.2.

$$\begin{aligned}
\langle M\rangle(\omega,\tilde{\omega}) &= tr(\tilde{A}^{COSY}\overbrace{\left|i^{ZF}\right\rangle\!\left\langle i^{ZF}\right| \left|j^{ZF}\right\rangle\!\left\langle j^{ZF}\right| \left|\rho_j^0\right\rangle\!\left\langle\rho_k^0\right| \left|k^{ZF}\right\rangle\!\left\langle k^{ZF}\right| \left|l^{ZF}\right\rangle\!\left\langle l^{ZF}\right|}^{B^{COSY}} M) \tag{xxx}\\
&= tr(\tilde{A}^{COSY}\left|i^{ZF}\right\rangle\left\langle i^{ZF}\right| \left|\rho_i^0\right\rangle\!\left\langle\rho_l^0\right| \left|l^{ZF}\right\rangle\left\langle l^{ZF}\right| M) \tag{xxxi}\\
&= \tilde{A}^{COSY}\sum_h \left\langle h^{ZF}\middle|i^{ZF}\right\rangle\left\langle i^{ZF}\right| \left|\rho_i^0\right\rangle\!\left\langle\rho_l^0\right| \left|l^{ZF}\right\rangle\left\langle l^{ZF}\right| M \left|h\right\rangle \tag{xxxii}\\
&= \tilde{A}^{COSY}\left\langle i^{ZF}\right| \left|\rho_i^0\right\rangle\!\left\langle\rho_l^0\right| \left|l^{ZF}\right\rangle\left\langle l^{ZF}\right| M \left|i^{ZF}\right\rangle \tag{xxxiii}\\
& \tag{xxxiv}
\end{aligned}$$

---

[f] This follows from the fact that summing over all projections leads to the resolution of unity

This leads us to the conclusion that we can read out the off diagonal ($i \neq l$) terms of the state/magnetisation overlap. This is particularly useful, because it allows us to in principle investigate superpositions of ZULF states.

B.3 Conceptual guides

Symmetry breaking

A common misconception around the full spherical symmetry of the ZULF hamiltonian is the conflation of symmetries of the hamiltonian with symmetries of the state. Where the hamiltonian (after preparation) is fully spherically symmetric, the state is, due to its directional preparation, not so. This is the reason why we can get a ZULF signal in the first place. This is not as surprising as it might seem at first glance, because it is equivalent to high-field NMR, where the cylindrical symmetry of the potential is contrasted with the direction of the spin, which can be tilted away from the axis of symmetry. The key takeway is thus that symmetries of the hamiltonian do not give rise to symmetries of solutions, but rather to conserved quantities within those solutions. For the case of ZULF NMR the conserved quantity is the angular momentum F. While F is conserved we should not be confused by the notion of transitions between $F = n$ and $F = n \pm 1$. Those transitions are not real changes in F, but rather a observed phase difference between the two energy levels. This phase difference can be picked up by measuring in a different basis than F.